OPTICS

Disorder-induced optical transition from spin Hall to random Rashba effect

Elhanan Maguid, Michael Yannai, Arkady Faerman, Igor Yulevich, Vladimir Kleiner, Erez Hasman*

Disordered structures give rise to intriguing phenomena owing to the complex nature of their interaction with light. We report on photonic spin-symmetry breaking and unexpected spin-optical transport phenomena arising from subwavelength-scale disordered geometric phase structure. Weak disorder induces a photonic spin Hall effect, observed via quantum weak measurements, whereas strong disorder leads to spin-split modes in momentum space, a random optical Rashba effect. Study of the momentum space entropy reveals an optical transition upon reaching a critical point where the structure's anisotropy axis vanishes. Incorporation of singular topology into the disordered structure demonstrates repulsive vortex interaction depending on the disorder strength. The photonic disordered geometric phase can serve as a platform for the study of different phenomena emerging from complex media involving spin-orbit coupling.

The study of light-matter interaction in nanoscale disordered media produces fascinating results and new phenomena owing to the unforeseen nature of manipulating light on a subwavelength scale. One can typically discern two types of disorder in a medium: (i) spatial disorder in crystal lattices, perturbed periodic potential, and the presence of impurities; or (ii) disorder that involves spin-orbit interaction, such as in a disordered magnetic dipole system.

Disordered structures in condensed-matter physics can exhibit quantum interference effects, such as Anderson localization (*1*). Also observed is the weak localization effect involving the suppression of conductivity due to multiscattering, which occurs during the transport of electrons through a disordered system. Enhancement of conductivity, or weak antilocalization, has also been observed in disordered systems with spin-orbit coupling. The opposite behavior of the localization and antilocalization effects is due to coherent backscattering that originates from constructive or destructive quantum interference, respectively. In the latter, the π phase difference arises from a Berry phase—a geometric phase that accumulates upon traveling in a non-Euclidean state space, the Bloch sphere (*2*). Another manifestation of spin-orbit interaction is the extrinsic electronic spin-Hall effect, which originates from the scattering of electrons by impurities (random defects) (*3*, *4*).

In photonics, disordered structures have resulted in anomalous photonic transport, light localization, and focusing (*5*–*7*). Anderson localization of light induced by randomization of the local refractive index in a layered structure on a subwavelength scale has been observed (*8*). By implementing a nanoantenna array with random local resonances, a unique stochastic light transport medium was introduced (*9*).

Here, we study the unexplored phenomena arising from a disordered Pancharatnam-Berry phase (geometric phase), which provides a photonic spin-orbit interaction mechanism, i.e., a coupling of the photon's spin to its extrinsic linear and orbital angular momentum (OAM) (*10*, *11*). The geometric phase pick-up constitutes an intrinsic property of the scatterers, arranged on a subwavelength lattice structure. Spin-symmetry breaking was observed from a subwavelength disordered geometric phase structure in contrast to the naïve assumption of effective medium theory, expecting a behavior of a homogeneous medium. We find that enhancing the disorder enables the observation of distinct regimes of spin-optical transport at the transition from an ordered system to a weakly disordered, and further to a strongly disordered, system.

The geometric phase accumulation, which arises from space-variant manipulation of the polarization state of light, traverses various geodesic paths on the Poincaré sphere and is equivalent to half the area of the geodesic triangle defined by these paths (*2*, *12*). This type of polarization manipulation is enabled by tiling a surface with anisotropic nanoantennas, arranged according to an on-demand space-variant orientation profile $\theta(x, y)$, thus forming a geometric phase metasurface (GPM) (*12*). In general, a metasurface can be described as an array of nanoantennas, serving as local phase shifters. Such nanopatterned structures were used for complex light manipulations and as a platform to study various physical phenomena (*13*–*16*). In particular, a GPM converts an incident circularly polarized beam of light into a beam of opposite spin, imprinted with a geometric phase $\phi_g(x, y) = -2\sigma\theta(x, y)$, where $\sigma = \pm 1$ denotes the incident polarization helicity, right (σ_+) or left (σ_-) circular polarization, respectively. A GPM possessing broken inversion symmetry may induce a spin-split momentum redirection of $\Delta k = 2\sigma\Omega$, where $\Omega = \nabla\theta$, resulting in spin-split dispersion known as the optical Rashba effect (*16*–*19*).

We investigate disordered geometric phase metasurfaces (DGPMs) that manifest peculiar spin-dependent photonic transport at different disorder strengths at on-axis illumination. Weak geometric phase disorder gives rise to a photonic spin-Hall effect (PSHE) observed within a diffraction-limited area about the center of momentum space (Fig. 1B). By incrementally increasing the disorder, a critical point is approached at which the PSHE abruptly vanishes, and numerous spin-split modes are observed—a random optical Rashba effect (Fig. 1C). These random modes span the entire momentum space, and therefore their scattering strength is quantified by measuring the momentum space image entropy. By introducing a topological charge to the disordered geometric phase, unexpected photonic transport is observed. The dynamics of the

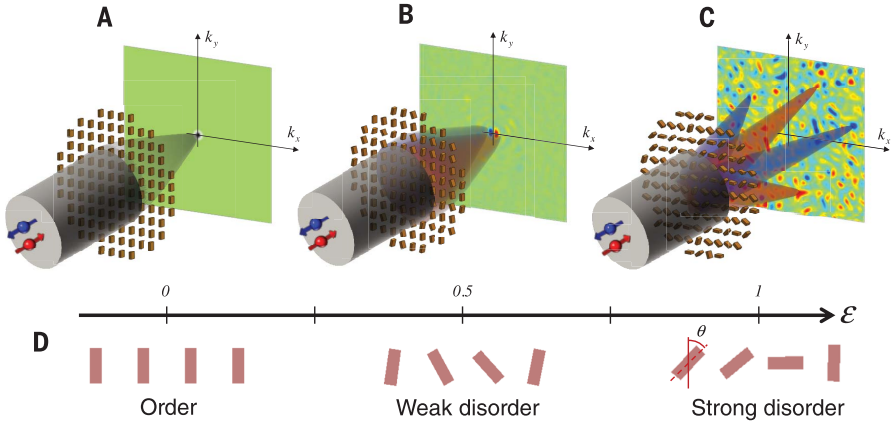

Fig. 1. Photonic transitions from weak to strong disorder. (**A**) Ordered, (**B**) weakly disordered, and (**C**) strongly disordered geometric phase structures demonstrating PSHE (B) and random optical Rashba effect (C). (**D**) Illustration of DGPM sections for various disorder parameter (ε) values. Here θ is the orientation of each nanoantenna, ranging from $-\varepsilon\pi/2$ to $\varepsilon\pi/2$. Red and blue colors represent spin-up and spin-down states, respectively.

Micro and Nanooptics Laboratory, Faculty of Mechanical Engineering, and Russell Berrie Nanotechnology Institute, Technion–Israel Institute of Technology, Haifa 3200003, Israel.
***Corresponding author. Email: mehasman@technion.ac.il**

PSHE and the distorted topology beam were experimentally studied via quantum weak measurement technique (*20*). Vortex repulsion depending on the disorder strength, which leads to confined trajectories of the generic singularities, is presented.

To demonstrate the photonic spin-symmetry breaking, we designed Si-based subwavelength DGPMs (*21*) and investigated the spin-dependent photonic transport for various disorder strengths (Fig. 2A) (*22*). The DGPM is characterized by the disorder parameter ε ($0 < \varepsilon \leq 1$), which indicates the range of the random rotation $\theta_\varepsilon(x, y)$, obeying a uniform distribution function $f_\varepsilon(\theta) = \{1/\varepsilon\pi, -\varepsilon\pi/2 < \theta \leq \varepsilon\pi/2, 0$ otherwise$\}$. Therefore, at the critical point $\varepsilon = 1$ (a fully disordered DGPM), the structure's anisotropy axis is vanished and the geometric phase covers the full 2π range of local phase pickup, as illustrated by the Poincaré sphere (Fig. 2B). When $\varepsilon = 0$, the orientation of the nanoantennas is homogeneous, hence the element acts as a half-waveplate performing a spin-flip—conversion from spin-up (σ_+) to spin-down (σ_-) and vice versa, as was verified experimentally (Fig. 2D). The DGPMs of different ε were illuminated with circularly polarized light from a 633-nm He-Ne laser, and measured the emerging far-field spin-flipped component. A bright diffraction-limited spot was observed in the center of momentum space for disorder parameter values up to $\varepsilon = 0.95$, in agreement with calculations (Fig. 2D and fig. S2). When the disorder parameter approached unity ($\varepsilon = 1$), the bright spot vanished, and numerous modes spanning the momentum space were observed. To quantify this transitional effect, we derived the momentum space image entropy from the

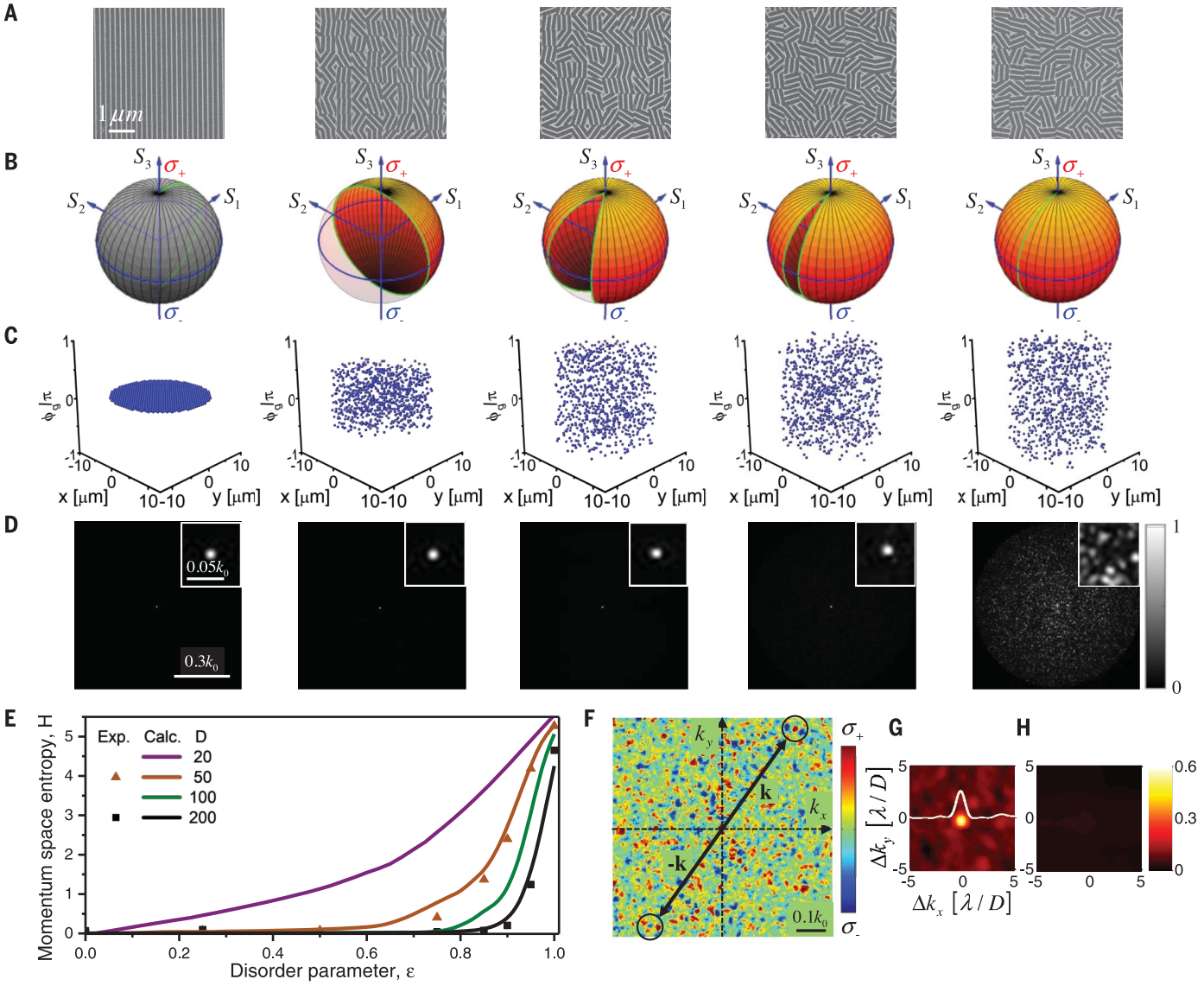

Fig. 2. Entropy and spin-split modes in momentum space. (**A**) Scanning electron microscopy images of the DGPMs for different disorder parameter (ε) values (0, 0.5, 0.85, 0.95 and 1, left to right). (**B**) Illustration of the geometric phase pick-up via the Poincaré sphere. The phase pick-up is equal to half the area of the geodesic triangle (colored). (**C**) Spatial phase distributions of the disordered geometric phase for different ε values and for a specific spin state. (**D**) Measured momentum space intensity distributions of the spin-flipped component illuminated with spin-up. Insets show enlargements of the momentum space central region. Here, k_0 is the wave number for a wavelength of 633 nm. (**E**) Calculated (lines) and measured (symbols) momentum space entropies for various DGPMs of different aperture sizes (D) ranging from 20 μm (purple) to 200 μm black). (**F**) Measured difference of momentum space intensities $I_{\sigma_+}(\mathbf{k}) - I_{\sigma_-}(\mathbf{k})$ for $\varepsilon = 1$. Spin-up (σ_+) and spin-down (σ_-) are shown in red and blue, respectively. Black arrows highlight selected examples of correspondent spin-split modes. (**G** and **H**) measured correlation functions of the momentum space intensities $I_{\sigma_+}(\mathbf{k})$ and $I_{\sigma_-}(-\mathbf{k})$ (G), and for $I_{\sigma_+}(\mathbf{k})$ and $I_{\sigma_-}(\mathbf{k})$ (H). A single peak, the width of which is equal to the diffraction-limited spot, is clearly observed in (G).

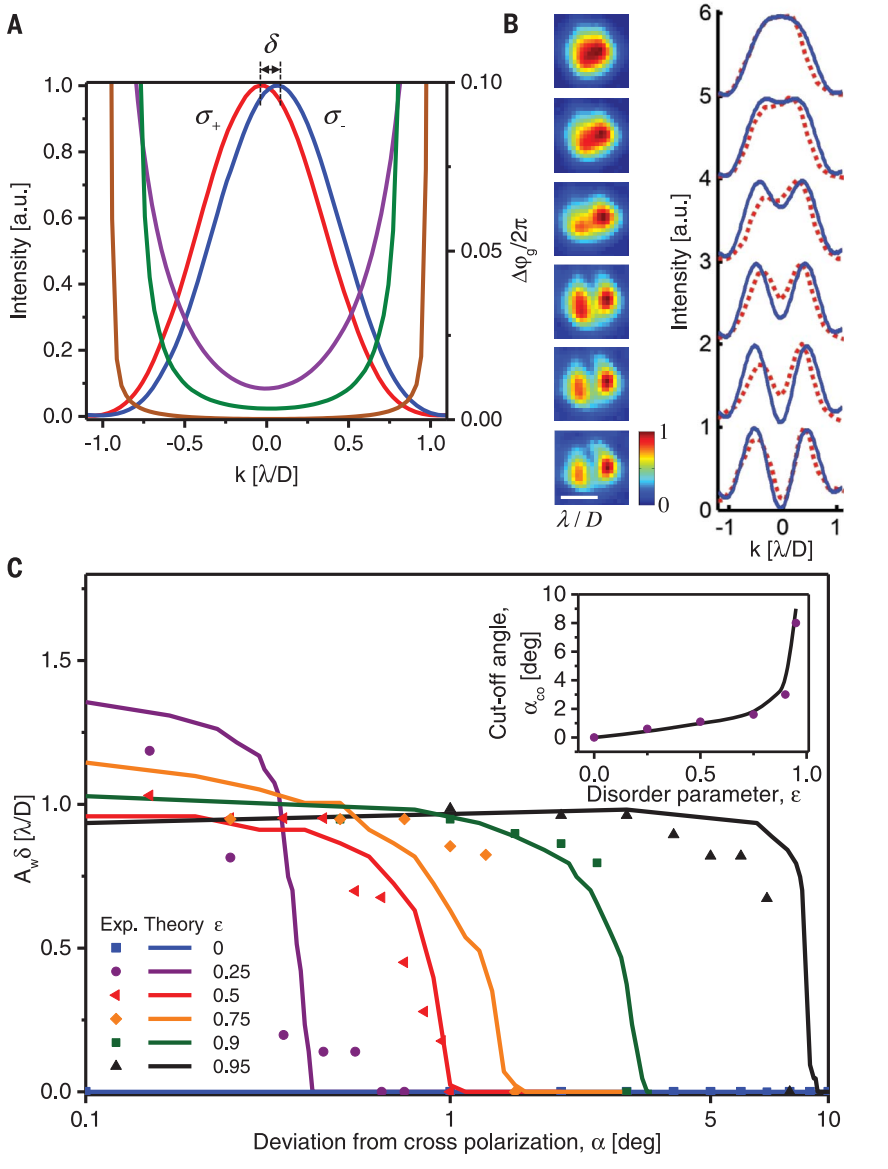

Fig. 3. Weak measurement of PSHE. (**A**) Calculated momentum space intensity and the related phase cross sections demonstrating the PSHE obtained from a weakly disordered GPM. Red and blue lines depict spin-up and spin-down intensities, respectively. The unamplified separation (δ) is highlighted. Brown, green, and purple lines depict the phase between the spin states at ε of 0.5, 0.85, and 0.9, respectively. (**B**) Experimental enhancement of the PSHE obtained via weak measurement for a DGPM of ε = 0.5. Images are taken at various polarizer-analyzer angles ranging from 0 (cross-polarized, bottom) to 1 degree (top). The corresponding cross sections are depicted in red (measurements) and blue (calculation). (**C**) Calculated (lines) and measured (symbols) amplification of the PSHE obtained via weak measurement for various disorder parameter values and as a function of the polarizer-analyzer deviation from cross polarization. Inset depicts the polarizer-analyzer cut-off angle, defined by unity amplification ($A_w = 1$), as a function of the disorder parameter.

far-field measurements and observed a steep increase in the vicinity of full disorder, in agreement with the calculation for different structures' diameters (Fig. 2E) (*22*).

We experimentally observed spin-split modes in the momentum space (Fig. 2F). To show that these modes originate from a spin-orbit interaction due to the geometric phase, we calculated and measured the correlation functions $\langle I_{\sigma_+}(\mathbf{k}) I_{\sigma_-}(\mathbf{k}+\Delta\mathbf{k})\rangle$, and $\langle I_{\sigma_+}(\mathbf{k}) I_{\sigma_-}(-\mathbf{k}+\Delta\mathbf{k})\rangle$; where $I_{\sigma_+}(\mathbf{k}), I_{\sigma_-}(\mathbf{k})$ are the spin-flipped momentum space intensity patterns for each incident spin-state, and $I_{\sigma_-}(-\mathbf{k})$ is the flipped-momentum with respect to $I_{\sigma_-}(\mathbf{k})$. Here, $\Delta\mathbf{k}$ denotes a displacement in the momentum space. The correlation functions demonstrate the spin-symmetry breaking $I_{\sigma_+}(\mathbf{k}) \neq I_{\sigma_-}(\mathbf{k})$ and time-reversal symmetry $I_{\sigma_+}(\mathbf{k}) = I_{\sigma_-}(-\mathbf{k})$ (Fig. 2, G and H). These two symmetry postulates provide evidence of the existence of a photonic Rashba effect (*16*, *19*, *22*). The fully disordered geometric phase gave rise to a random optical Rashba effect, which can be interpreted as a superposition of numerous effective Rashba potentials Ω_i. The modified Helmholtz equation describing the disordered system is given by $(\nabla^2 + k^2 + \sigma\Omega_i k)\psi_i = 0$, where $\sigma\Omega_i k$ is a random correction term and ψ_i is the spin-eigenvector of the electric field (*19*). This equation can be written in first-order approximation as $(\nabla^2 + K_i^2)\psi_i = 0$, where $K_i = k + \sigma\,\Omega_i$ is the generalized momentum, resulting in random spin-split modes in the momentum space (Fig. 2F and fig. S10).

Far-field Jones calculus of the field emerging from a DGPM revealed a PSHE (*22*–*24*), spin-dependent beam displacement (δ), two orders of magnitude smaller than the diffraction-limit for $0 < \varepsilon < 1$ (Fig. 3A). Moreover, a geometric phase difference that varies with the disorder strength is obtained; higher disorder results in a larger phase difference between opposite helicities. Calculations show that even for an extremely small disorder parameter, a PSHE is still obtained (fig. S13). The experimental observation of the effect was achieved by using quantum weak measurement techniques to enable amplification of the subdiffraction-limit beam shift (*23*). Amplification of a weak value of the measured observable $\hat{A}$ is achieved by applying preselection and postselection polarization projections, $|\psi_{pre}\rangle$ and $|\psi_{post}\rangle$ states, resulting in an amplified value $A_w = \langle\psi_{pre}|\hat{A}|\psi_{post}\rangle / \langle\psi_{pre}|\psi_{post}\rangle$ (*20*). We measured a separation on the order of the diffraction-limited spot ($A_w\delta$), where A_w roughly equals 80, for a DGPM with on-axis illumination (Fig. 3, A and B, and fig. S14). Moreover, we obtained the dependence of the separation $A_w(\alpha)\delta$ on the deviation angle α from cross-polarization arrangement at the postselection polarizer (Fig. 3C). The dynamic range of the deviation defined by the cut-off angle $\alpha_{co}(\varepsilon)$, where amplification decreases up to the minimum $A_w(\alpha_{co}) \approx 1$, was found to be sensitive to the disorder parameter (Fig. 3C, inset). This provides a proof of concept for a new technique to evaluate the disorder strength in nanoscale structures involving spin-orbit interaction.

The use of geometric phase as a platform for the study of disordered systems enables the incorporation of a different topology into the DGPM in the form of optical vortices (*10*, *11*). The twisted DGPMs of different ε were oriented according to the relation $\tilde{\theta}_\varepsilon(x,y) = \theta_\varepsilon(x,y) + l\varphi/2$ to obtain a distorted topological charge, where φ is the azimuthal angle and l is the topological charge (Fig. 4, A and B). Figure 4C depicts the measured far-field patterns emerging from these structures for different disorder parameter values and for a topological charge of $l = 2$. For an unperturbed helical phase, a doughnut-shaped intensity pattern is observed. Gradually adding disorder to this topology reveals a distorted intensity pattern that vanishes completely when ε = 1. This approach to the critical point is observed via the momentum space entropy for different topological charges

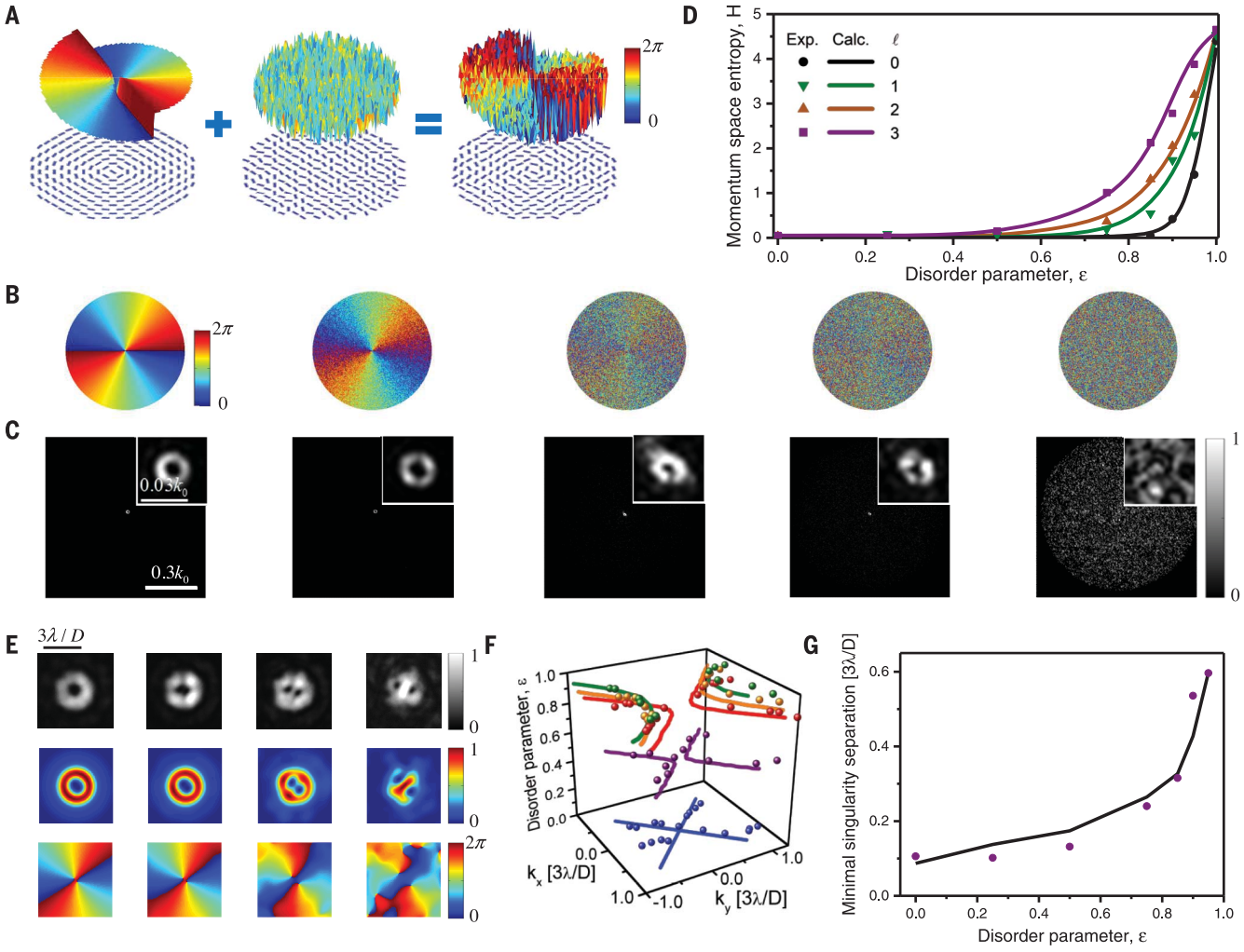

Fig. 4. Twisted disordered geometric phase and weak measurement of singular points. (**A**) Illustration of twisted DGPM, combining a helical phase with a disordered phase to obtain a distorted helical phase profile. (**B** and **C**) The distorted helical phase profiles for $l = 2$(B), and the measured momentum space intensities (C) for different disorder parameter values $\varepsilon = 0,\ 0.25,\ 0.85,\ 0.95$ and 1 (left to right). Insets show enlargements of the momentum space central region. (**D**) Calculated (lines) and measured (symbols) momentum space entropies for various DGPMs of different topological charges, ranging from $l = 0$ (black) to $l = 3$ (purple). (**E**) Intensity profiles of the weak measurement of the singularities' separation for $\varepsilon = 0, 0.5, 0.85$, and 0.95 (left to right) and a topological charge $l = 2$; top, measured intensity; middle, calculated intensity; and bottom, calculated phase. Polarizer-analyzer was set to a fixed angle of 2° deviation from the spin-flip state. (**F**) Calculated (lines) and measured (dots) trajectories in the momentum space of the generic singularities as a function of the disorder parameter, achieved by varying the postselection polarizer-analyzer. (**G**) Calculation (line) and measurements (dots) of the minimal separation between the singular points as a function of ε, corresponding to the data in (F). The scale of $3\lambda/D$ is used to normalize the momentum space with respect to the diffraction limit of a beam of $l = 2$.

(Fig. 4D) (*22*). For weak disorder ($0.25 < \varepsilon < 0.95$), dark fringes that split the intensity doughnut are observed, behaving as a fractional topological charge–Berry dislocation (*25*).

We study the instability of distorted high-order singularities. By the projection of orthogonal spin-states—the spin-flipped distorted vortex and the spin-maintained Gaussian beam—onto an elliptical polarization state, weak measurement of singular points is obtained. The breaking of high-order singularities into generic dislocation and its dynamics was studied by adjusting the polarization-analyzer from circular to elliptical. Figure 4E depicts the breaking of an OAM-carrying beam of $l = 2$ into generic singularities of $l = 1$ at a specific postselection, demonstrating disorder strength-dependent separation–repulsive vortex interaction (see fig. S15 for $l = 3$). Adjustment of the postselection analyzer results in well-defined trajectories of the repulsive singularities (Fig. 4F), revealing a correlation between the minimal distance of the singularities and the disorder strength (Fig. 4G). The interaction between geometric phase disorder and singularities provides the route for the creation of effective vortex repulsion to generate nanoscale singular structures.

The photonic disordered geometric phase can serve as a platform for the study of different quantum phase transitions and vacuum fluctuations of electromagnetic radiation, emerging from complex media involving spin-orbit interaction and topological defects (figs. S8 and S9) (*26*, *27*).

REFERENCES AND NOTES

1. *50 Years of Anderson Localization*, E. Abrahams, Ed. (World Scientific, Singapore, 2010).
2. M. V. Berry, *Proc. R. Soc. London Ser. A* **392**, 45–57 (1984).
3. M. I. Dyakonov, V. I. Perel, *Phys. Lett. A* **35**, 459–460 (1971).
4. J. Sinova, S. O. Valenzuela, J. Wunderlich, C. H. Back, T. Jungwirth, *Rev. Mod. Phys.* **87**, 1213–1260 (2015).
5. A. Apostol, A. Dogariu, *Phys. Rev. Lett.* **91**, 093901 (2003).
6. M. Segev, Y. Silberberg, D. Christodoulides, *Nat. Photonics* **7**, 197–204 (2013).
7. D. S. Wiersma, *Nat. Photonics* **7**, 188–196 (2013).
8. H. H. Sheinfux *et al.*, *Science* **356**, 953–956 (2017).

9. A. Pors, F. Ding, Y. Chen, I. P. Radko, S. I. Bozhevolnyi, *Sci. Rep.* **6**, 28448 (2016).
10. K. Y. Bliokh, F. Nori, *Phys. Rep.* **592**, 1–38 (2015).
11. K. Y. Bliokh, F. J. Rodríguez-Fortuño, F. Nori, A. V. Zayats, *Nat. Photonics* **9**, 796–808 (2015).
12. Z. Bomzon, G. Biener, V. Kleiner, E. Hasman, *Opt. Lett.* **27**, 1141–1143 (2002).
13. V. M. Shalaev, *Nat. Photonics* **1**, 41–48 (2007).
14. E. T. F. Rogers *et al.*, *Nat. Mater.* **11**, 432–435 (2012).
15. X. Yin, Z. Ye, J. Rho, Y. Wang, X. Zhang, *Science* **339**, 1405–1407 (2013).
16. N. Shitrit *et al.*, *Science* **340**, 724–726 (2013).
17. E. I. Rashba, *Sov. Phys. Solid State* **2**, 1109 (1960).
18. K. Ishizaka *et al.*, *Nat. Mater.* **10**, 521–526 (2011).
19. N. Dahan, Y. Gorodetski, K. Frischwasser, V. Kleiner, E. Hasman, *Phys. Rev. Lett.* **105**, 136402 (2010).
20. Y. Aharonov, D. Z. Albert, L. Vaidman, *Phys. Rev. Lett.* **60**, 1351–1354 (1988).
21. D. Lin, P. Fan, E. Hasman, M. L. Brongersma, *Science* **345**, 298–302 (2014).
22. See supplementary materials.
23. O. Hosten, P. Kwiat, *Science* **319**, 787–790 (2008).
24. K. Y. Bliokh, D. Smirnova, F. Nori, *Science* **348**, 1448–1451 (2015).
25. M. V. Berry, R. G. Chambers, M. D. Large, C. Upstill, J. C. Walmsley, *Eur. J. Phys.* **1**, 154–162 (2000).
26. S. Ducci, P. L. Ramazza, W. González-Viñas, F. T. Arecchi, *Phys. Rev. Lett.* **83**, 5210–5213 (1999).
27. C. Riek *et al.*, *Science* **350**, 420–423 (2015).

ACKNOWLEDGMENTS

This research was supported by the Israel Science Foundation (ISF). The fabrication was performed at the Micro-Nano Fabrication and Printing Unit (MNF&PU), Technion. All results are reported in the main paper and supplementary materials.

SUPPLEMENTARY MATERIALS

www.sciencemag.org/content/358/6369/1411/suppl/DC1
Supplementary text
Figs. S1 to S19
References (*28*, *29*)

4 September 2017; accepted 14 November 2017
10.1126/science.aap8640

Disorder-induced optical transition from spin Hall to random Rashba effect

Elhanan Maguid, Michael Yannai, Arkady Faerman, Igor Yulevich, Vladimir Kleiner and Erez Hasman

Science **358** (6369), 1411-1415.
DOI: 10.1126/science.aap8640

Phase transition of scattered light

Disordered structures can give rise to intriguing scattering phenomena owing to the unpredictable nature of their interaction with light. Using subwavelength-scale disordered metasurfaces, Maguid *et al.* observed a phase transition in how the light is scattered as a function of disorder. Weak disorder induced a photonic spin Hall effect, whereas strong disorder led to spin-split modes in momentum space, a random optical-Rashba effect. Thus, designed photonic structure could offer a versatile platform to study similar phenomena in complex solid-state systems.

Science, this issue p. 1411